Camera Calibration using a Collimator System

Shunkun Liang, Banglei Guan✉, Zhenbao Yu, Pengju Sun, and Yang Shang

College of Aerospace Science and Engineering, National University of Defense Technology, China.

Abstract. Camera calibration is a crucial step in photogrammetry and 3D vision applications. In practical scenarios with a long working distance to cover a wide area, target-based calibration methods become complicated and inflexible due to site limitations. This paper introduces a novel camera calibration method using a collimator system, which can provide a reliable and controllable calibration environment for cameras with varying working distances. Based on the optical geometry of the collimator system, we prove that the relative motion between the target and camera conforms to the spherical motion model, reducing the original 6DOF relative motion to 3DOF pure rotation motion. Furthermore, a closed-form solver for multiple views and a minimal solver for two views are proposed for camera calibration. The performance of our method is evaluated in both synthetic and real-world experiments, which verify the feasibility of calibration using the collimator system and demonstrate that our method is superior to the state-of-the-art methods. Demo code is available at *https://github.com/LiangSK98/CollimatorCalibration*

Keywords: Camera calibration · Collimator system · Spherical motion · Closed-form solver · Minimal solver

1 Introduction

Geometric camera calibration determines the mapping between 3D rays in space and 2D image pixels. Various vision applications, such as simultaneous localization and mapping(SLAM) [6], structure from motion(SfM) [32], and pose estimation [11, 12], rely on camera parameters as inputs. The close-range calibration methods using a planar target represent the prevailing techniques in 3D vision applications [5, 26, 33, 35, 46]. In some special outdoor scenarios, such as long-range depth estimation [45] and monitoring of wind turbine blades [10], the cameras achieve a long working distance and a large field of view. The traditional target-based calibration methods [3, 37, 46] may face challenges, such as needing large targets, moving or arranging targets over a wide area, and dealing with varying and unstable lighting conditions. While constructing a 3D calibration field can offer precise calibration data [34, 40, 42], its operational complexity and limited adaptability present significant challenges. In addition, the collimator is

✉ Corresponding author. `guanbanglei12@nudt.edu.cn`

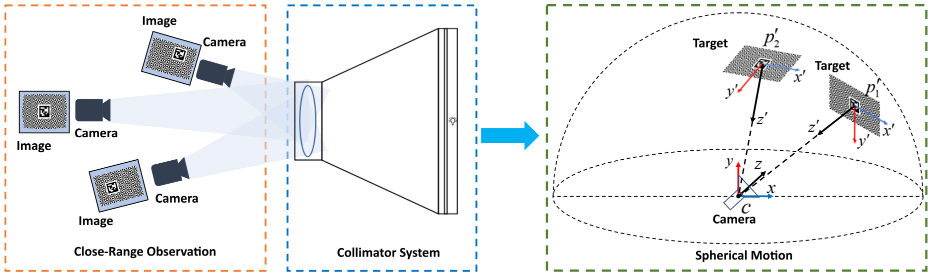

Fig. 1: Diagram of the collimator-based calibration method. From the inherent optical geometric properties of the collimator, the relative motion between the target and camera can be proved to conform to the spherical motion model.

commonly used to generate calibration targets [7]. Traditional collimator-based methods need to measure the direction of collimated rays using a goniometer or theodolite, which makes the calibration process challenging, and measurement errors directly impact the accuracy [41, 43, 44].

In this paper, we design a novel collimator system with a structured calibration pattern on its reticle, and a novel calibration algorithm based on the collimator images is proposed. Our method only requires the camera to observe the pattern from our collimator system at a few (at least two) different orientations. Fig. 1 illustrates this method. We briefly analyze the geometric optical property of the collimator and illustrate the angle invariance of any point pairs on the pattern. By leveraging angle invariance, we prove that the relative motion between the calibration target and the camera conforms to a spherical motion model. This constraint effectively reduces the original 6DOF general motion to the 3DOF pure rotation motion. Furthermore, we propose a novel calibration method using the collimator system. Compared with the target-based methods, more geometric constraints can be derived from the collimator, leading to higher accuracy. Compared to traditional collimator-based methods, our method is more flexible as it eliminates the need for direction measurement.

Our primary contributions can be summarized as follows: (1) We propose a novel camera calibration method using a collimator system. The entire calibration process can be implemented with multiple close-range observations and does not require the known direction of collimated rays. (2) We prove that the relative motion between the calibration target and the camera conforms to the spherical motion model. This constraint effectively reduces the number of motion parameters to be estimated. (3) A closed-form solver for multiple views and a minimal solver for two views are proposed based on the spherical motion constraint. Moreover, the degenerate case of the proposed solvers is proved.

2 Related Work

Camera calibration is a crucial subject in 3D vision and continues to be actively researched. The literature on camera calibration introduces a wide range of algorithms and toolboxes [3–5,22,26,33,35,46]. To ensure the highest accuracy for calibration, targets with known structures are usually used for camera calibration. Various calibration targets have been proposed, including 3D targets [37], 2D targets [13,18] and 1D targets [47]. In some practical applications where no calibration target is available, the camera calibration can be performed by establishing the correspondence between images during the movement of the camera, which is known as self-calibration [8,9,16,19,28,31]. Among these options, the target-based close-range calibration method is widely used.

In outdoor long-range measurement applications [10,45], the camera has a long working distance to measure the long-distance targets. Thus, the close-range calibration methods are impractical due to the site limitation. A commonly employed approach involves constructing a calibration field, which serves as a known structure for the calibration [21,25,29,34,40,42]. Oniga *et al*. [29] lay markers on buildings to calibrate cameras mounted on UAV. Shang *et al*. [34] proposed a high-precision calibration method by placing several markers near the ground. Additionally, Klaus *et al*. [23] proposed using stars as distant targets to estimate camera parameters.

The collimator is also commonly used to provide 2D-3D correspondence for camera calibration in the laboratory [2,20,41,44]. Previous collimator-based methods proposed to use goniometer or theodolite to obtain the direction of collimated rays and then estimate the camera parameters [41,43]. The collimator-based method offers both accuracy and flexibility in the limited space, but a high-precision goniometer or theodolite is expensive. To address this, Yuan *et al*. [44] designed a multiple pinhole mask for the collimator to generate the collimated rays with known directions. However, the accuracy of calibration is sensitive to machining errors. Bauer *et al*. [2] proposed a calibration method using a diffractive optical element (DOE). The angle between the laser beam and the camera can then be estimated to determine the camera parameters.

3 Collimator System

This section introduces the designed collimator system and shows that the equivalent relative motion between the calibration target and the camera conforms to a spherical motion model.

3.1 Scheme of Collimator System

The collimator is an optical instrument that can produce collimated rays and plays an important role when adjusting other optical instruments. A collimator consists of essential components such as a light source, a reticle, and an optical lens, as illustrated in Fig. 2. The reticle is a thin glass located on the focal plane of the collimator. The generation of collimated rays can be regarded as the inverse process of imaging a target at infinity onto the focal plane. Specifically, a point on the lens's focal plane will generate collimated rays, which can be regarded as the target at infinity. Therefore, cameras with varying focal lengths can consistently and accurately observe the target through the collimator at a close range.

In this paper, we design a collimator system for camera calibration. A star-based pattern, proposed by Thomas *et al.* [33], is attached to the reticle of the collimator as the calibration target. The star-based pattern offers richer gradient information for improving feature extraction accuracy. Similar to the plane-based calibration method [35, 46], the star-based pattern provides 2D-3D correspondences for camera calibration. Our collimator system is portable with a size of about $200mm \times 170mm \times 300mm$. The collimator system is designed to provide a reliable and controllable calibration environment for some special scenarios like inappropriate illumination, limited space, and long-range cameras. However, printed targets face challenges in these scenarios. When calibrating a camera, we only need to capture the target from multiple orientations through the lens of the collimator, which is as easy as the printed targets method.

3.2 Spherical Motion Model

In this section, we prove that the relative motion between the calibration target and the camera conforms to the spherical motion model. Firstly, we briefly analyze the geometric property of the collimator. As shown in Fig. 2, let us note two arbitrary points P_1 and P_2 on the reticle of the collimator. Rays emitted from P_1 and P_2 pass through the collimator lens, generating two parallel beams observed by cameras denoted as C_1 and C_2 with arbitrary poses. The propagation routes of the two beams are visually distinguished by red and blue lines in Fig. 2. Obviously, the angle between two lines observed by the two cameras is equal, that is, $\theta_1 \equiv \theta_2 \equiv \theta$. We can obtain a property that the two rays observed by the cameras always maintain a constant angle, regardless of the poses of observing cameras. We refer to this property as the angle invariance.

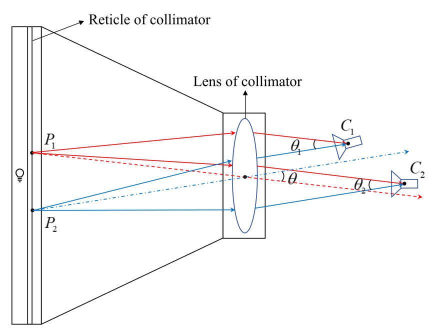

Fig. 2: Diagram of collimator system. The geometric property of the collimator system leads to the angle invariance of any point pair on the reticle.

Next, we show that this setup, where a camera moves around a collimator system and captures images, is theoretically equivalent to the capture setting where the camera is fixed, but the images are moving around the camera spherically. This can be derived from the angle invariance. For convenience in introducing our derivation process, we treat the camera as a fixed reference coordinate, and assume that the calibration target moves relative to the camera in space. The angle invariance allows us to infer that when the target performs a specific motion in space, the angular distance between any point pair on the target always remains constant. The angular distance means the angle between two vectors from the origin (camera optical center) to two points. By arbitrarily selecting a pair of points $\mathbf{P}_i$ and $\mathbf{P}_j$ on the target and transforming them, we can establish the following equation

$$\angle\left(\mathbf{P}_i, \mathbf{P}_j\right) = \angle\left(\mathbf{R}\left(\mathbf{P}_i + \mathbf{t}\right), \mathbf{R}\left(\mathbf{P}_j + \mathbf{t}\right)\right), \tag{1}$$

where $\mathbf{R}$ is rotation matrix and $\mathbf{t}$ is translation vector. From the rotation invariance [39] that a pair of 3D points are jointly rotated about the origin, their angular distance remains constant. We have $\angle\left(\mathbf{R}\left(\mathbf{P}_i + \mathbf{t}\right), \mathbf{R}\left(\mathbf{P}_j + \mathbf{t}\right)\right) = \angle\left(\mathbf{P}_i + \mathbf{t}, \mathbf{P}_j + \mathbf{t}\right)$. Thus, the angle invariance is maintained when the calibration target is arbitrarily rotated about the origin. To make $\angle(\mathbf{P}_i, \mathbf{P}_j)) = \angle(\mathbf{P}_i + \mathbf{t}, \mathbf{P}_j + \mathbf{t})$ hold for any pair of points on the target, the translation vector must be a $\mathbf{0}$ vector ($\mathbf{t} = [0, 0, 0]^T$). The proof is given in the *supplementary material*. Therefore, the calibration target performs pure rotation motion with respect to the origin (*i.e.* camera optical center). Such pure rotational motion is a typical spherical motion.

The spherical motion can be visualized in Fig. 1. In the spherical motion model, the calibration target exhibits only rotational motion with a fixed distance relative to the camera. We establish a local coordinate on the target, where the z'-axis aligns with the ray between the camera coordinate system c and calibration target coordinate system p'. Inspired by [38], the relative pose between the calibration target and camera can be mathematically represented as

$$\mathbf{T}_{cp'} = \begin{pmatrix} \mathbf{R}_{cp'} & \mathbf{t}_{cp'} \\ \mathbf{0}_{1\times3} & 1 \end{pmatrix}, \tag{2}$$

where $\mathbf{R}_{cp'} \in SO(3)$, $\mathbf{t}_{cp'} = (0, 0, -r)^T$ and r is the radius of spherical motion. We usually establish the origin of the coordinate system p on the upper left corner of the calibration pattern. Therefore, there is a relative translation $\mathbf{t}_{p'p} = (x, y, 0)$ between the coordinate systems p' and p. Furthermore, the transformation matrix between camera c and calibration target p is expressed as follows:

$$\mathbf{T}_{pc} = \left[\begin{pmatrix} \mathbf{R}_{cp'} & \mathbf{t}_{cp'} \\ \mathbf{0}_{1\times3} & 1 \end{pmatrix}\begin{pmatrix} \mathbf{I}_{3\times3} & \mathbf{t}_{p'p} \\ \mathbf{0}_{1\times3} & 1 \end{pmatrix}\right]^{-1} = \begin{pmatrix} \mathbf{R}_{pc} & -\mathbf{R}_{pc}\mathbf{t}_{cp} \\ \mathbf{0}_{1\times3} & 1 \end{pmatrix}, \tag{3}$$

where $\mathbf{R}_{pc} = \mathbf{R}_{cp'}^T$ and $\mathbf{t}_{cp} = \mathbf{t}_{p'p} + \mathbf{t}_{cp'} = (x, y, -r)^T$. $\mathbf{t}_{cp}$ determines the position of the camera in the calibration target coordinate system. Note that $\mathbf{t}_{cp}$ is a fixed value and has nothing to do with the pose of the calibration target. Given the constraint from the spherical motion, the original 6DOF general motion is limited to a 3DOF pure rotation motion.

4 Calibration Method

The spherical motion constraint effectively reduces the number of motion parameters to be estimated. In this section, we show how to calibrate camera parameters using a set of collimator images. A closed-form solver for multiple views and a minimal solver for two views are proposed.

4.1 Geometric Constraints

We use the well-known pinhole model to model cameras. The mapping from a 3D point $\mathbf{P} = (X, Y, Z)^T$ to an image point $\mathbf{p} = (u, v)^T$ is computed as

$$s\widetilde{\mathbf{p}} = \mathbf{K}[\mathbf{R} \mid \mathbf{t}]\widetilde{\mathbf{P}}, \text{ with } \mathbf{K} = \begin{bmatrix} f_x & \gamma & c_x \\ 0 & f_y & c_y \\ 0 & 0 & 1 \end{bmatrix}, \tag{4}$$

where s is an arbitrary scale factor, $(\mathbf{R}, \mathbf{t})$ is the camera pose with respect to the calibration target coordinate, and $\mathbf{K}$ is the camera intrinsic matrix. $\widetilde{\mathbf{p}} = [u, v, 1]^T$ and $\widetilde{\mathbf{P}} = [X, Y, Z, 1]^T$ denote the homogeneous coordinate forms of points $\mathbf{p}$ and $\mathbf{P}$, respectively. The intrinsic matrix $\mathbf{K}$ consists of five parameters: the focal length (f_x, f_y), the principal point (c_x, c_y) and skew factor γ.

Without loss of generality, we assume the planar target is on the plane $Z = 0$ of the world coordinate system. The transformation between the image plane and calibration target plane can be constrained by a 3×3 homography matrix, denoted as $\mathbf{H}$. For perspective projection, the homography matrix $\mathbf{H}$ depends on the image pose $(\mathbf{R}, \mathbf{t})$ and intrinsic matrix $\mathbf{K}$:

$$\mathbf{H} = \begin{bmatrix} \mathbf{h}_1 & \mathbf{h}_2 & \mathbf{h}_3 \end{bmatrix} = \lambda \mathbf{K} \begin{bmatrix} \mathbf{r}_1 & \mathbf{r}_2 & \mathbf{t} \end{bmatrix}, \tag{5}$$

where λ is an arbitrary scalar, $\mathbf{r}_i$ is the i-th columns of $\mathbf{R}$. Given an image of the calibration target, the homography matrix $\mathbf{H}$ can be estimated using the plane point correspondences. Combining Eq. (3) and Eq. (5), we can get

$$\mathbf{M} = \begin{bmatrix} \mathbf{r_1} & \mathbf{r_2} & -\mathbf{R}\mathbf{t}_{cp} \end{bmatrix} = \frac{1}{\lambda}\mathbf{K}^{-1}\mathbf{H}. \tag{6}$$

Using the knowledge that $\mathbf{R}$ is an orthogonal matrix, we have

$$\mathbf{H}^T\mathbf{K}^{-T}\mathbf{K}^{-1}\mathbf{H} = \lambda^2 \begin{bmatrix} 1 & 0 & -x \\ 0 & 1 & -y \\ -x & -y & \|\mathbf{t}_{cp}\|^2 \end{bmatrix}. \tag{7}$$

There are 8 parameters to be estimated, 5 for intrinsic matrix and 3 for $\mathbf{t}_{cp} = (x, y, -r)^T$. For each given image, Eq. (7) provides 5 independent constraints. Theoretically, a minimum of two images can completely solve all unknown parameters. In the next two subsections, we give a closed-form solver for $N (N > 2)$ collimator images and a minimal solver for two collimator images.

4.2 Closed-form Solver for Multiple Views

When there are more than two collimator images for calibration, we model the problem as a linear system and propose a closed-form solution. Suppose that the homography matrices $\mathbf{H}_i (i = 1, ..., N)$ have been estimated for all images. The transformations between images i and j can be expressed as

$$\mathbf{H}_j^{-1}\mathbf{H}_i = \frac{\lambda_i}{\lambda_j}\mathbf{M}_j^{-1}\mathbf{M}_i. \tag{8}$$

For the matrix $\mathbf{M}$ of each image, we can calculate the determinant as

$$\begin{aligned}|\mathbf{M}| &= \left|\mathbf{r}_1\ \mathbf{r}_2\ -\mathbf{R}\mathbf{t}_{cp}\right| = \left|\mathbf{r}_1\ \mathbf{r}_2\ -x\mathbf{r}_1 - y\mathbf{r}_2 + r\mathbf{r}_3\right| \\ &= -x\left|\mathbf{r}_1\ \mathbf{r}_2\ \mathbf{r}_1\right| - y\left|\mathbf{r}_1\ \mathbf{r}_2\ \mathbf{r}_2\right| + r\left|\mathbf{r}_1\ \mathbf{r}_2\ \mathbf{r}_3\right| = r,\end{aligned} \tag{9}$$

where r is a non-zero fixed value. Using the fact that $\det(\mathbf{M}_j^{-1}\mathbf{M}_i) = 1$, we have $\lambda_{ij} = \lambda_i/\lambda_j = \sqrt[3]{|\mathbf{H}_j^{-1}\mathbf{H}_i|}$. Then, we choose the image with the most feature points observed as the base image. For convenience, here the first image is selected as the base image and we get $\lambda_{i1} = \sqrt[3]{|\mathbf{H}_j^{-1}\mathbf{H}_1|}$. By inverting Eq. (7) of image i, we get

$$\mathbf{H}_i^{-1}\mathbf{K}\mathbf{K}^T\mathbf{H}_i^{-T} = \frac{1}{\lambda_i^2 r^2}\begin{bmatrix} r^2+x^2 & xy & x \\ xy & r^2+y^2 & y \\ x & y & 1 \end{bmatrix}. \tag{10}$$

Substitute $\lambda_i = \lambda_{i1}\lambda_1$ into Eq. (10), we get

$$\mathbf{H}_i^{-1}\mathbf{K}\mathbf{K}^T\mathbf{H}_i^{-T} = \frac{1}{\lambda_{i1}^2}\mathbf{A},\ \text{with}\ \mathbf{A} = \begin{bmatrix} \frac{r^2+x^2}{(\lambda_1 r)^2} & \frac{xy}{(\lambda_1 r)^2} & \frac{x}{(\lambda_1 r)^2} \\ \frac{xy}{(\lambda_1 r)^2} & \frac{r^2+y^2}{(\lambda_1 r)^2} & \frac{y}{(\lambda_1 r)^2} \\ \frac{x}{(\lambda_1 r)^2} & \frac{y}{(\lambda_1 r)^2} & \frac{1}{(\lambda_1 r)^2} \end{bmatrix}. \tag{11}$$

Let us define a 6-vector $\mathbf{a}$ to represent matrix $\mathbf{A}$:

$$\mathbf{a} = (A_{11}, A_{12}, A_{13}, A_{22}, A_{23}, A_{33})^T,$$

where A_{mn} is the value of m-th row and n-th column of matrix $\mathbf{A}$. Let

$$\mathbf{W} = \begin{bmatrix} {c_x}^2 + {f_x}^2 + \gamma^2 & c_x c_y + f_y\gamma & c_x \\ c_x c_y + f_y\gamma & {c_y}^2 + {f_y}^2 & c_y \\ c_x & c_y & 1 \end{bmatrix}. \tag{12}$$

Note that $\mathbf{W}$ is a symmetric matrix and can be defined by a 5-vector:

$$\mathbf{w} = (W_{11}, W_{12}, W_{13}, W_{22}, W_{23})^T,$$

where W_{mn} is the value of m-th row and n-th column of matrix $\mathbf{W}$. Obviously, Eq. (11) represents a linear system of equations involving the unknowns $[\mathbf{w}^T, \mathbf{a}^T]^T$. Combining Eqs. (11) and (12), we can get the following equations for each image:

$$\begin{bmatrix} \mathbf{V} & -\lambda_{i1}^2\mathbf{I}_{5\times5} \end{bmatrix}\begin{bmatrix} \mathbf{w} \\ \mathbf{a} \end{bmatrix} = \mathbf{b}, \tag{13}$$

with

$$\begin{aligned}\mathbf{V} &= [\mathbf{v}_{11}, \mathbf{v}_{12}, \mathbf{v}_{13}, \mathbf{v}_{22}, \mathbf{v}_{23}]^T, \\ \mathbf{v}_{mn} &= [h_{m1}h_{n1}, h_{m1}h_{n2} + h_{m2}h_{n1}, h_{m1}h_{n3} + h_{m3}h_{n1}, \\ &\qquad h_{m2}h_{n2}, h_{m2}h_{n3} + h_{m3}h_{n2}], \\ \mathbf{b} &= -[h_{13}h_{13}, h_{13}h_{23}, h_{13}h_{33}, h_{23}h_{23}, h_{23}h_{33}]^T,\end{aligned}$$

where h_{mn} denotes the value of m-th row and n-th column of matrix $\mathbf{H}^{-1}$. Given $N(N>2)$ collimator images, we can stack N such equations as Eq. (13) together in matrix form:

$$\mathbf{D}\begin{bmatrix}\mathbf{w}\\ \mathbf{a}\end{bmatrix}=\mathbf{b}, \tag{14}$$

where $\mathbf{D}$ is a $5N\times 11$ matrix. The closed-form solution of Eq. (14) is given by

$$\begin{bmatrix}\mathbf{w}\\ \mathbf{a}\end{bmatrix}=(\mathbf{D}^T\mathbf{D})^{-1}\mathbf{D}^T\mathbf{b}. \tag{15}$$

Once $\mathbf{w}$ and $\mathbf{a}$ are estimated, we can calculate all camera intrinsic parameters and optical center $\mathbf{t}_{cp}$ by decomposing $\mathbf{W}$ and $\mathbf{A}$ respectively:

$$\begin{aligned}
&c_x=W_{13},\quad c_y=W_{23},\quad f_y=\sqrt{W_{22}-{c_y}^2},\\
&\gamma=(W_{12}-c_xc_y)/f_y,\quad f_x=\sqrt{W_{11}-{c_x}^2-\gamma^2},\\
&x=A_{13}/A_{33},\quad y=A_{23}/A_{33},\\
&r=-\sqrt{(A_{11}/A_{33})-(A_{13}/A_{33})^2}.
\end{aligned}$$

Subsequently, the rotation matrix of each image can be calculated with Eq. (5):

$$\mathbf{r}_1=(1/\lambda)\mathbf{K}^{-1}\mathbf{h}_1,\quad \mathbf{r}_2=(1/\lambda)\mathbf{K}^{-1}\mathbf{h}_2,\quad \mathbf{r}_3=\mathbf{r}_1\times\mathbf{r}_2, \tag{16}$$

where $\lambda=(\left\|\mathbf{K}^{-1}\mathbf{h}_1\right\|+\left\|\mathbf{K}^{-1}\mathbf{h}_2\right\|)/2$. Finally, a singular value decomposition for re-orthogonalizing the rotation matrix $\mathbf{R}=[\mathbf{r}_1,\mathbf{r}_2,\mathbf{r}_3]$ is required.

4.3 Minimal Solver for Two Views

When only two collimator images are used for calibration, the rank of the coefficient matrix in Eq. (14) is determined to be 10. Solving rank-deficient equations presents a complex challenge. To address this issue, we construct a nonlinear equation system and propose a novel approach that utilizes the hidden variable technique [14] to estimate the unknowns in the minimum configuration.

Estimation of $\mathbf{W}=\mathbf{K}^{-T}\mathbf{K}^{-1}$ is the core of calibration. Note that $\mathbf{W}$ is a symmetric matrix, defined by a 6-vector $\mathbf{w}=(W_{11},W_{12},W_{13},W_{22},W_{23},W_{33})^T$. We can extract the following 5 constraints from Eq. (7)

$$\mathbf{v}_{12}^T\mathbf{w}=0 \tag{17}$$

$$(\mathbf{v}_{11}^T-\mathbf{v}_{22}^T)\mathbf{w}=0 \tag{18}$$

$$\mathbf{v}_{13}^T\mathbf{w}+x\mathbf{v}_{11}^T\mathbf{w}=0 \tag{19}$$

$$\mathbf{v}_{23}^T\mathbf{w}+y\mathbf{v}_{11}^T\mathbf{w}=0 \tag{20}$$

$$\mathbf{v}_{33}^T\mathbf{w}-\left\|\mathbf{t}_{cp}\right\|^2\mathbf{v}_{11}^T\mathbf{w}=0. \tag{21}$$

$\mathbf{v}_{mn}$ can be calculated as following:

$$\begin{aligned}
\mathbf{v}_{mn}=&[h_{1m}h_{1n},h_{1m}h_{2n}+h_{1n}h_{2m},h_{1m}h_{3n}+h_{1n}h_{3m}\\
&h_{2m}h_{2n},h_{2m}h_{3n}+h_{2n}h_{3m},h_{3m}h_{3n}]^T,
\end{aligned}$$

where h_{mn} denotes the value of m-th row and n-th column of matrix $\mathbf{H}$. Given only 2 collimator images, we can obtain 10 independent equations for 8 unknowns. The hidden variable technique [14] is employed to solve the above polynomial equations. Combining Eqs. (19) to (21), we have

$$(\mathbf{v}_{13}^T + \mathbf{v}_{23}^T + \mathbf{v}_{33}^T)\mathbf{w} + c\mathbf{v}_{11}^T\mathbf{w} = 0, \tag{22}$$

where $c = (x + y - \|\mathbf{t}_{cp}\|^2)$. We first select constraints Eqs. (17), (18) and (22) to establish a new polynomial equation system. Next, we treat c as a hidden variable, and the complete set of equations can be expressed in matrix form as

$$\mathbf{C}(c)\mathbf{w} = 0, \text{ with } \mathbf{C}(c) = \begin{bmatrix} \mathbf{v}_{12}^T \\ (\mathbf{v}_{11}^T - \mathbf{v}_{22}^T) \\ (\mathbf{v}_{13}^T + \mathbf{v}_{23}^T + \mathbf{v}_{33}^T) + c\mathbf{v}_{11}^T \end{bmatrix}, \tag{23}$$

where the coefficient matrix $\mathbf{C}(c)$ contains the hidden variable c. Two images provide 6 equations for solving c, and $\mathbf{C}(c)$ is a 6×6 matrix. Since the equation system $\mathbf{C}(c)\mathbf{w} = 0$ must have at least one nontrivial solution for $\mathbf{w}$, the determinant of $\mathbf{C}(c)$ is equal to zero. The equation, $\det(\mathbf{C}(c)) = 0$, is a polynomial of degree 2 in terms of c, which can be efficiently solved using a straightforward root-finding algorithm. Substituting the known value of c into the constraint equations Eqs. (17), (18) and (22), we obtain six constraint equations about $\mathbf{w}$. The least squares method is then employed to solve these linear equations and compute the optimal $\mathbf{w}$ up to scale. Once $\mathbf{w}$ is estimated, the intrinsic matrix $\mathbf{K}$ can be calculated using the Cholesky factorization [15].

4.4 Bundle Adjustment

Bundle adjustment jointly refines the camera intrinsic $\mathbf{K}$, lens distortion coefficients $\mathbf{d}$, the rotation matrix of the i-th image $\mathbf{R}_i$ and camera optical center $\mathbf{t}_{cp}$. In cases of moderate lens distortion, it is typical to initialize the distortion coefficient to $\mathbf{0}$ and estimate them in the bundle adjustment step [36]. Given a set of N images, each with M corresponding 2D image points, we establish a cost function aimed at minimizing the re-projection error. The cost function is expressed as follows:

$$\min_{\mathbf{X}} \sum_{i}^{N} \sum_{j}^{M} \rho \left(\|\pi\left(\mathbf{K}, \mathbf{d}, \mathbf{R}_i, \mathbf{t}_{cp}, \mathbf{P}_{ij}\right) - \mathbf{p}_{ij}\|^2 \right), \tag{24}$$

where $\mathbf{X} = (\mathbf{K}, \mathbf{d}, \mathbf{R}_i, \mathbf{t}_{cp})$ is the parameter to be refined. $\mathbf{P}_{ij}$ is the j-th 3D pattern point of i-th image and corresponds to the 2D image point $\mathbf{p}_{ij}$. $\pi(\cdot)$ projects the world points to image according to Eq. (4). $\rho(\cdot)$ is the Cauchy cost function. As is common, we optimize Eq. (24) with the Levenberg-Marquardt (LM) method [27], which is implemented in some excellent frameworks [1].

Note that the camera optical center is fixed at $\mathbf{t}_{cp}$ with the spherical motion constraint. However, for general motion, the camera optical center is free. Therefore, when calibrating the camera using collimator images, the number of motion parameters to be refined is reduced from $6N$ to $3N + 3$.

4.5 Degenerated Configuration

We prove a degenerate configuration where additional images cannot provide more constraints about the camera intrinsic parameter.

Proposition 1. *If the calibration target rotates only around an axis that is parallel to the z axis and intersects the target plane at $(x, y, 0)^T$, the newly added image cannot provide additional constraints on the camera intrinsic parameters.*

Due to space limitations, the proof is provided in the *supplementary material*.

5 Evaluation and Results

In this section, we first evaluate the robustness and accuracy of the proposed algorithm on synthetic data. Then, we calibrate the camera and evaluate the effectiveness of the proposed method using real collimator images.

5.1 Synthetic Data Experiments

In the synthetic data experiment, we evaluate the performance of the proposed algorithm. We simulate the process of calibrating predefined camera parameters using synthetic images that conform to the spherical motion model. The proposed is compared with the following algorithms:

- `Zhang` [46] is a plane-based algorithm and suitable for general 6DOF motion.
- `Bouguet` [3] is a calibration toolbox and suitable for general 6DOF motion. Unlike `Zhang`, `Bouguet` computes the focal length using the orthogonal vanishing points constraint.
- `Hartley` [17] is a self-calibration method based on a pure rotating camera, which is specifically suitable for the 3DOF spherical motion model.

We define a virtual camera with the following parameters: $f_x = f_y = 1000, c_x = 542, c_y = 478, \gamma = 0.01$, radial distortion coefficients $d_1 = 0.1, d_2 = -0.2$, and the image size is set to 1080×960 pixels. The calibration target is a planar pattern containing 11×8 points, each square size of $30mm \times 30mm$. The target maintains a spherical motion with a radius of $700mm$ relative to the camera. The camera optical center in the target coordinate system is $t_{cp} = [150, 105, -700]^T mm$, and the camera's orientation is arbitrary. Given the camera parameters and poses, the planar target points are projected onto images. Finally, zero-mean Gaussian noise with σ standard deviation is added to 2D image points.

Evaluation of Calibration. In this experiment, we seek to evaluate the performance of the algorithms in solving camera parameters. For the four algorithms, we perform two steps of solving initial value and bundle adjustment to obtain camera parameters. Firstly, we compare the performance of the mentioned algorithms as the noise level increases. The noise level varies from 0 to 3.0 pixels, and we use 15 images to calibrate the camera. For each noise level, we conducted 200 trials and calculated the average errors. As shown in Fig. 3, calibration error increases linearly with the noise level. Compared with the other three algorithms, ours shows greater robustness to noise. Additionally, at a noise

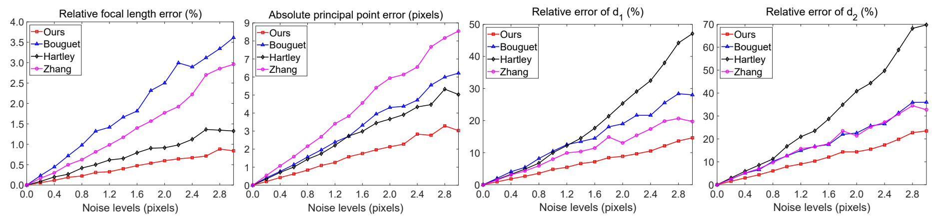

Fig. 3: Comparison of calibration errors with increasing noise level.

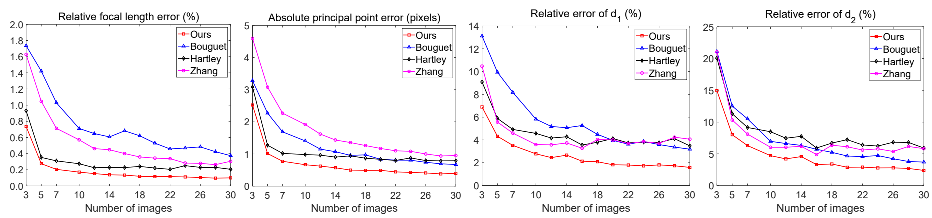

Fig. 4: Comparison of calibration errors with the number of images increases.

level of 0.5 pixels, we evaluate the performance with respect to the number of calibration images. The image count ranged from 3 to 30, with 200 trials conducted for each quantity. The results are illustrated in Fig. 4. A significant decrease in error is observed when increasing the number of images from 3 to 5. Both Fig. 3 and Fig. 4 show that our algorithm outperforms other algorithms in robustness and accuracy. We believe that our algorithm benefits from the consideration of both spherical motion and planar homography constraints, along with reducing optimization variables. Due to space limitations, the additional comparison results of the initial value estimation are shown in the *supplementary material*.

Sensitivity of imperfect spherical motion. The low-cost collimators exhibit an inferior parallelism, which is reflected in the fact that the relative motion between the target and camera is not a perfect spherical motion. This experiment evaluates the sensitivity of initial value estimation with respect to imperfect spherical motion. We add zeros-mean Gaussian noise with standard deviation from $0mm$ to $30mm$ to $\mathbf{t}_{cp}$ to replicate this imperfection. We use 15 images and add a noise level of 0.5 pixels to the image points. For each noise level, a total of independent 500 trials are conducted and the average errors are computed. The sensitivity analysis results are shown in Fig. 5. Noise has no impact on `Bouguet` and `Zhang`, because they do not rely on the spherical motion constraint. As the noise increases, calibration errors of `Ours` and `Hartley` increase gradually. Notably, `Hartley` is significantly influenced by noise, whereas `Ours` displays superior robustness. Even with noise levels below $15mm$ (equivalent to 2.143% of the spherical radius), our algorithm remains superior to the alternatives.

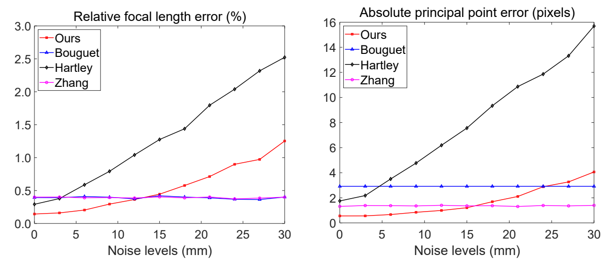

Fig. 5: Sensitivity analysis of imperfect spherical motion.

Table 1: Comparison of calibration and pose estimation error results (pixels).

Number	Zhang [46]		Bouguet [3]		Hartley [17]		Ours	
	ϵ_{calib}	ϵ_{eval}	ϵ_{calib}	ϵ_{eval}	ϵ_{calib}	ϵ_{eval}	ϵ_{calib}	ϵ_{eval}
2	0.1842	0.1545	0.1739	**0.1518**	-	-	0.1739	0.1519
5	0.2316	0.1245	0.2202	**0.1236**	-	0.2577	0.2203	**0.1236**
10	0.1923	0.1231	0.1912	0.1232	-	0.1986	0.1951	**0.1222**
15	0.1775	0.1221	0.1718	0.1232	-	0.1791	0.1779	**0.1216**
20	0.1773	0.1225	0.1722	0.1221	-	0.1871	0.1778	**0.1207**

5.2 Real Images Experiments

In real image experiments, we verify the effectiveness of our collimator system for calibration and evaluate the performance of the proposed algorithm.

Calibration and Accuracy Evaluation. Following the experimental methodology utilized in previous studies [13,30], we design a pose estimation experiment to evaluate the accuracy of camera calibration quantitatively. A $8mm$ camera captures images from our collimator system and a practical printed pattern. Calibration is performed using the collimator images and a subset of the printed pattern images, while the remaining printed pattern images are used to evaluate the calibration results. After obtaining the camera parameters from the calibration images, the pose of each evaluation image can be determined using absolute pose estimation [24].In our setup, a quarter of the corner points on the printed pattern are used for pose estimation, and the remaining points are used for evaluation. By re-projecting the evaluation corner points onto the image with the camera parameters and the calculated pose, we can evaluate the calibration quality based on the re-projection error. A total of 200 printed pattern images are used to evaluate the calibration. The calibration uses 2, 5, 10, 15, and 20 images. The re-projection error of the calibration and evaluation images are donated as ϵ_{calib} and ϵ_{eval}, respectively.

The comparison results of the four algorithms are shown in Tab. 1. Due to the limited degrees of freedom, our calibrated re-projection error (ϵ_{calib}) is slightly higher. However, `Ours` exhibits the lowest re-projection error in evaluation images compared to alternative methods, indicating that our method achieves more precise camera parameters. The `Hartley` method only uses the correspondence of 2D points in images, which makes it impossible to calculate the re-projection

Table 2: Comparison of calibration results using 20 images in a real camera.

	Printed	Collimator			
	Bouguet [3]	Zhang [46]	Bouguet [3]	Hartley [17]	Ours
f_x	2384.5	2380.8	2369.2	2644.6	2388.3
f_y	2386.3	2379.8	2368.9	2646.0	2387.9
c_x	1209.8	1222.1	1221.1	1214.6	1221.0
c_y	1008.2	1008.4	1009.8	1012.7	1009.6
k_1	-0.0843	-0.0899	-0.0908	-0.0754	-0.0900
k_2	0.0819	0.0912	0.0892	0.1181	0.0954
ϵ_{calib}	0.1513	0.1773	0.1722	-	0.1778
ϵ_{eval}	0.1225	0.1225	0.1221	0.1871	0.1207

Table 3: Comparison of epipolar rectification error results (pixels).

Number	Zhang [46]		Bouguet [3]		Hartley [17]		Ours	
	mean	std	mean	std	mean	std	mean	std
2	0.0846	0.0406	**0.0770**	0.0220	-	-	**0.0770**	0.0229
5	0.0809	0.0307	0.0764	0.0214	0.0832	0.0397	**0.0762**	0.0211
10	0.0773	0.0234	0.0758	0.0213	0.0854	0.0509	**0.0757**	0.0208
15	0.0782	0.0266	0.0771	0.0253	0.0837	0.0522	**0.0756**	0.0207
20	0.0772	0.0252	0.0768	0.0253	0.0818	0.0365	**0.0756**	0.0208

error of the calibration images directly. In cases with only two images, `Zhang` and `Bouguet` commonly depend on beneficial assumptions, such as $\gamma = 0$. `Ours` achieves comparable evaluation errors without the need for such assumptions.

Additionally, the `Bouguet` toolbox is also used to calculate camera parameters from printed pattern images that are not included in the evaluation. We use 20 images for calibration and 200 for evaluation. The estimated camera parameters and error comparison are shown in Tab. 2. The second column is a good reference. The lower evaluation error indicates that our method outperforms the alternative and validates the effectiveness of using the collimator image for calibration. It can be expected that the calibration parameters are not significantly different. Therefore, even a minor improvement holds considerable significance.

Then, we evaluate the performance of all methods using epipolar rectification error, which has not been optimized. Given the camera parameters from different methods, we calculate the epipolar rectification error (in pixels) for 300 pairs of printed evaluation images. The mean and standard deviation of the errors are shown in Tab. 3. Moreover, the result using `Bouguet` with 20 printed pattern images is (0.0772, 0.0259) pixels. It is observed that as the number of calibration images increases, the error stabilizes. The results indicate improved accuracy in the collimator image and highlight the beneficial impact of the spherical constraint on accuracy.

Multiple Cameras Calibration with a Same Collimator. In this experiment, we evaluate our method on multiple cameras with the same collimator. We used the cameras with $12mm$, $16mm$, $25mm$, and $35mm$ focal lengths of lenses. The calibration images are captured from the same collimator, as shown in Fig. 6 and left of Fig. 1. As the focal length increases, the more pixels a single

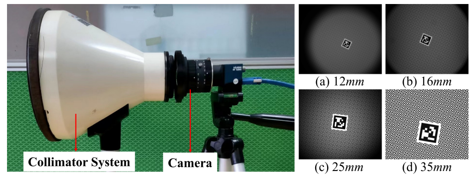

Fig. 6: Calibration image sample obtained from the collimator.

Table 4: Comparison of calibration results with different focal length lense (pixels).

	Zhang [46]	Bouguet [3]	Hartley [17]	Ours
$12mm$	0.2273	0.2225	0.3404	**0.2174**
$16mm$	0.2994	0.2591	0.4182	**0.2536**
$25mm$	0.3133	0.3078	0.4195	**0.2923**
$35mm$	0.3289	0.3348	0.7272	**0.3118**

square occupies. Cameras with different focal lengths can observe the calibration target through our collimator system in a limited space.

Similar to the evaluation approach in the previous experiment, we segregate all collimator images into calibration and evaluation sets. For each lens, we use 20 images for calibration and 200 for evaluation. The results are listed in Tab. 4. The proposed algorithm demonstrates the lowest re-projection error for lenses with varying focal lengths among the evaluation images. The re-projection error tends to increase with the increase of focal length. We believe that the main reason is that the longer the lens's focal length, the fewer points observed. More importantly, this experiment confirms the effectiveness of our collimator system and the proposed method. Moreover, we provide a spherical motion verification experiment in *supplementary material*.

6 Conclusion

This paper presents a novel camera calibration method using a designed collimator system. Based on the optical geometry of the collimator system, we prove that the relative motion between the target and the camera conforms to a spherical motion. Furthermore, we propose a closed-form solver for multiple views and a minimal solver for two views for camera calibration. Our collimator-based method effectively combines the advantages of close-range calibration using a collimator and flexibility using a planar calibration target. We validate the effectiveness of using only collimator images to calibrate the camera. Synthetic and real data experiments demonstrate that the calibration accuracy of the proposed method is superior to the state-of-the-art methods.

Limitations: When calibrating a fisheye camera, the distortion should be paid more attention rather than simply setting it to **0**. Future work will focus on cameras with significant distortion.

Acknowledgements

This research has been supported by the Hunan Provincial Natural Science Foundation for Excellent Young Scholars under Grant 2023JJ20045, and the National Natural Science Foundation of China under Grant 12372189. We thank Zijie Wang for useful discussion on the writing of the paper.

References

1. Agarwal, S., Mierle, K., Team, T.C.S.: Ceres Solver. `https://github.com/ceres-solver/ceres-solver`
2. Bauer, M., Grießbach, D., Hermerschmidt, A., Krüger, S., Scheele, M., Schischmanow, A.: Geometrical camera calibration with diffractive optical elements. Optics express **16**(25), 20241–20248 (2008)
3. Bouguet, J.Y.: Camera calibration toolbox for matlab. `http://robots.stanford.edu/cs223b04/JeanYvesCalib/index.html` (2004)
4. Bradski, G.: The opencv library. Dr. Dobb's Journal: Software Tools for the Professional Programmer **25**(11), 120–123 (2000)
5. Brown, D.C.: Close-range camera calibration. Photogramm. Eng **37**(8), 855–866 (1971)
6. Campos, C., Elvira, R., Rodríguez, J.J.G., M. Montiel, J.M., D. Tardós, J.: Orb-slam3: An accurate open-source library for visual, visual–inertial, and multimap slam. IEEE Transactions on Robotics **37**(6), 1874–1890 (2021)
7. Clarke, T.A., Fryer, J.G.: The development of camera calibration methods and models. The Photogrammetric Record **16**(91), 51–66 (1998)
8. Faugeras, O.D., Luong, Q.T., Maybank, S.J.: Camera self-calibration: Theory and experiments. In: IEEE European Conference on Computer Vision (ECCV). p. 321–334 (1992)
9. Führ, G., Jung, C.R.: Camera self-calibration based on nonlinear optimization and applications in surveillance systems. IEEE Transactions on Circuits and Systems for Video Technology **27**(5), 1132–1142 (2017)
10. Guan, B., Su, Z., Yu, Q., Li, Z., Feng, W., Yang, D., Zhang, D.: Monitoring the blades of a wind turbine by using videogrammetry. Optics and Lasers in Engineering **152**, 106901 (2022)
11. Guan, B., Zhao, J., Barath, D., Fraundorfer, F.: Minimal solvers for relative pose estimation of multi-camera systems using affine correspondences. International Journal of Computer Vision **131**(1), 324–345 (2023)
12. Guan, B., Zhao, J., Li, Z., Sun, F., Fraundorfer, F.: Relative pose estimation with a single affine correspondence. IEEE Transactions on Cybernetics **52**(10), 10111–10122 (2022)
13. Ha, H., Perdoch, M., Alismail, H., Kweon, I.S., Sheikh, Y.: Deltille grids for geometric camera calibration. In: IEEE International Conference on Computer Vision (ICCV). pp. 5354–5362 (2017)
14. Hartley, R., Li, H.: An efficient hidden variable approach to minimal-case camera motion estimation. IEEE Transactions on Pattern Analysis and Machine Intelligence **34**(12), 2303–2314 (2012)
15. Hartley, R., Zisserman, A.: Multiple View Geometry in Computer Vision. Cambridge University Press, 2 edn. (2004)

16. Hartley, R.I.: Self-calibration from multiple views with a rotating camera. In: European Conference on Computer Vision (ECCV). pp. 471–478 (1994)
17. Hartley, R.I.: Self-calibration of stationary cameras. International Journal of Computer Vision **22**(1), 5–23 (1997)
18. Heikkila, J.: Geometric camera calibration using circular control points. IEEE Transactions on Pattern Analysis and Machine Intelligence **22**(10), 1066–1077 (2000)
19. Herrera, D., Kannala, C.J., Heikkila, J.: Forget the checkerboard: Practical self-calibration using a planar scene. In: IEEE Winter Conference on Applications of Computer Vision (WACV). pp. 1–9. IEEE (2016)
20. Hieronymus, J.: Comparison of methods for geometric camera calibration. The International Archives of the Photogrammetry, Remote Sensing and Spatial Information Sciences **39**, 595–599 (2012)
21. Hu, H., Wei, B., Mei, S., Liang, J., Zhang, Y.: A two-step calibration method for vision measurement with large field of view. IEEE Transactions on Instrumentation and Measurement **71**, 1–10 (2022)
22. Kannala, J., Brandt, S.S.: A generic camera model and calibration method for conventional, wide-angle, and fish-eye lenses. IEEE Transactions on Pattern Analysis and Machine Intelligence **28**(8), 1335–1340 (2006)
23. Klaus, A., Bauer, J., Karner, K., Elbischger, P., Perko, R., Bischof, H.: Camera calibration from a single night sky image. In: IEEE Conference on Computer Vision and Pattern Recognition (CVPR). vol. 1, pp. I–I (2004)
24. Kneip, L., Furgale, P.: Opengv: A unified and generalized approach to real-time calibrated geometric vision. In: IEEE International Conference on Robotics and Automation (ICRA). pp. 1–8 (2014)
25. Liu, Z., Li, F., Li, X., Zhang, G.: A novel and accurate calibration method for cameras with large field of view using combined small targets. Measurement **64**, 1–16 (2015)
26. Lochman, Y., Liepieshov, K., Chen, J., Perdoch, M., Zach, C., Pritts, J.: Babelcalib: A universal approach to calibrating central cameras. In: IEEE International Conference on Computer Vision (ICCV). pp. 15253–15262 (2021)
27. Moré, J.J.: The levenberg-marquardt algorithm: implementation and theory. In: Numerical analysis: proceedings of the biennial Conference held at Dundee, June 28–July 1, 1977. pp. 105–116 (2006)
28. Nistér, D., Stewénius, H., Grossmann, E.: Non-parametric self-calibration. In: IEEE International Conference on Computer Vision (ICCV). vol. 1, pp. 120–127 (2005)
29. Oniga, V.E., Pfeifer, N., Loghin, A.M.: 3d calibration test-field for digital cameras mounted on unmanned aerial systems (uas). Remote Sensing **10**(12), 2017 (2018)
30. Peng, S., Sturm, P.: Calibration wizard: A guidance system for camera calibration based on modelling geometric and corner uncertainty. In: IEEE International Conference on Computer Vision (ICCV). pp. 1497–1505 (2019)
31. Pollefeys, M., Koch, R., Gool, L.V.: Self-calibration and metric reconstruction inspite of varying and unknown intrinsic camera parameters. International journal of computer vision **32**(1), 7–25 (1999)
32. Schönberger, J.L., Frahm, J.M.: Structure-from-motion revisited. In: IEEE Conference on Computer Vision and Pattern Recognition (CVPR). pp. 4104–4113 (2016)
33. Schöps, T., Larsson, V., Pollefeys, M., Sattler, T.: Why having 10,000 parameters in your camera model is better than twelve. In: IEEE Conference on Computer Vision and Pattern Recognition (CVPR). pp. 2532–2541 (2020)

34. Shang, Y., Sun, X., Yang, X., Wang, X., Yu, Q.: A camera calibration method for large field optical measurement. Optik - International Journal for Light and Electron Optics **124**, 6553–6558 (12 2013)
35. Sturm, P.F., Maybank, S.J.: On plane-based camera calibration: A general algorithm, singularities, applications. In: IEEE Conference on Computer Vision and Pattern Recognition (CVPR). vol. 1, pp. 432–437. IEEE (1999)
36. Triggs, B., McLauchlan, P.F., Hartley, R.I., Fitzgibbon, A.W.: Bundle adjustment—a modern synthesis. In: Vision Algorithms: Theory and Practice: International Workshop on Vision Algorithms. pp. 298–372. Springer (2000)
37. Tsai, R.: A versatile camera calibration technique for high-accuracy 3d machine vision metrology using off-the-shelf tv cameras and lenses. IEEE Journal on Robotics and Automation **3**(4), 323–344 (1987)
38. Ventura, J.: Structure from motion on a sphere. In: European Conference on Computer Vision (ECCV). vol. 9907, pp. 53–68 (2016)
39. Wang, C., Liu, Y., Wang, Y., Li, X., Wang, M.: Efficient and outlier-robust simultaneous pose and correspondence determination by branch-and-bound and transformation decomposition. IEEE Transactions on Pattern Analysis and Machine Intelligence **44**(10), 6924–6938 (2022)
40. Wang, Z., Wu, Z., Zhen, X., Yang, R., Xi, J., Chen, X.: A two-step calibration method of a large fov binocular stereovision sensor for onsite measurement. Measurement **62**, 15–24 (2015)
41. Wu, G., Han, B., He, X.: Calibration of geometric parameters of line array ccd camera based on exact measuring angle in lab. Optics and Precision Engineering **15**(10), 1628–1632 (2007)
42. Xiao, Z., Jin, L., Yu, D., Tang, Z.: A cross-target-based accurate calibration method of binocular stereo systems with large-scale field-of-view. Measurement **43**(6), 747–754 (2010)
43. Yuan, G., Zheng, L., Ding, Y., Zhang, H., Zhang, X., Liu, X., Sun, J.: A precise calibration method for line scan cameras. IEEE Transactions on Instrumentation and Measurement **70**, 1–9 (2021)
44. Yuan, G., Zheng, L., Sun, J., Liu, X., Wang, X., Zhang, Z.: Practical calibration method for aerial mapping camera based on multiple pinhole collimator. IEEE Access **8**, 39725–39733 (2019)
45. Zhang, K., Xie, J., Snavely, N., Chen, Q.: Depth sensing beyond lidar range. In: IEEE Conference on Computer Vision and Pattern Recognition (CVPR). pp. 1689–1697 (2020)
46. Zhang, Z.: A flexible new technique for camera calibration. IEEE Transactions on Pattern Analysis and Machine Intelligence **22**(11), 1330–1334 (2000)
47. Zhang, Z.: Camera calibration with one-dimensional objects. IEEE Transactions on Pattern Analysis and Machine Intelligence **26**(7), 892–899 (2004)